This is a preproof accepted article for *Mineralogical Magazine*
This version may be subject to change during the production process
DOI: 10.1180/mgm.2025.10147

REVISION I

Extending the mineralogy of U^{6+} (IV.): Uranyl phosphate sheet of novel topology in the crystal structure of ranunculite

JAKUB PLÁŠIL[1]*, NATHAN STECIUK[2], GWLADYS STECIUK[3], JIŘÍ SEJKORA[4], MARKÉTA JAROŠOVÁ[1], JAN ROHLÍČEK[1], SIMON PHILIPPO[5], IVAN NĚMEC[6], AND ALEXANDER MATTHIES[7]

[1] Institute of Physics of the CAS, v.v.i., Na Slovance 2, 182 00 Prague 8, Czech Republic

[2] Independent Researcher

[3] Université de Lorraine, CNRS, IJL, F-54000 Nancy, France

[4] Department of Mineralogy and Petrology, National Museum, Cirkusová 1740, 193 00 Prague 9, Czech Republic

[5] Section Minéralogie, Musée d'Histoire Naturelle, Rue Münster 25, Luxembourg, 2160, Luxembourg

[6] Department of Inorganic Chemistry, Faculty of Science, Charles University, Hlavova 8, 128 40, Prague 2, Czech Republic

[5] Independent Researcher

*Corresponding author; Email: plasil@fzu.cz

Abstract

Ranuculite is a rare supergene hydrated aluminum uranyl phosphate reliably reported only from the type locality – the Kobokobo pegmatite in the Sud-Kivu province, Democratic Republic of Congo; its structure has remained unknown until now. Based on 3D electron diffraction data, ranunculite is monoclinic, with a *C*-centered unit cell: a = 11.1812(7) Å, b = 17.9281(5) Å, c = 17.91548(16) Å, β = 98.350(4) °, and V = 3553.2(2) Å^3 (Z = 4). The structure (*C*2/*c*) was refined kinematically to R_1 = 0.4114 for 1697 unique observed reflections. The structure of ranunculite is based upon infinite uranyl-phosphate sheets of novel topology. The two-dimensional representation of the structural unit consists of hexagons (occupied by U^{6+}), pentagons (occupied by U^{6+}), squares (occupied by Al^{3+}) and triangles (occupied by P^{5+}). Those sheets are stacked perpendicular to **c**; the interplanar distance is about 9.5 Å. They result from the clusters of edge-sharing uranyl hexagonal and pentagonal bipyramids linked by Al-octahedra and PO_4 tetrahedra. The decoration of the sheets is unique but somewhat resembles the arrangement (of U-clusters, squares and triangles) observed in bijvoetite and lepersonnite topologies; the ring symbol is $6^1 5^1 4^2 3^2$. In the interlayer, there are two Al^{3+}-hosting sites (one [6]- and [5]-coordinated; the pyramidal one is only partially occupied), as well as isolated H_2O groups. There is an extensive network of hydrogen bonds; adjacent sheets are either held by hydrogen bonds only or by tetramers of Al-polyhedra when occupied (through shared O19). This arrangement most probably causes a

poor crystallinity of ranunculite (which gives rise to stacking faults observed in the powder diffraction data).

Keywords: ranunculite; aluminum uranyl phosphate; electron diffraction; crystal structure; sheet topology.

Introduction

The Kobokobo pegmatite in the Sud-Kivu province (Democratic Republic of Congo, Africa) was one of the largest beryllium deposits in the World during the 1950s, producing a tremendous amount of beryl, columbite, and cassiterite (Safiannikoff and Van Wambeke 1967; Van Wambeke 1987). It is one of the most interesting mineralogical localities known, mainly due to occurrences of rare uranium and thorium phosphates within this U-bearing quartz–albite–muscovite pegmatite. These minerals formed during the last evolutionary stages when the phosphate-rich solutions altered the primary Th- and Pb-rich uraninite and zircon. This pegmatite is a type locality for twelve actinoid-bearing phosphates, most of which contain Al^{3+} (Table 1). Despite some recent crystallographic studies conducted on the Kobokobo material deposited in museums, the structures of many of the Kobokobo minerals remain unknown. Here, we present a crystal structure determination on the rare uranyl phosphate ranunculite, originally described by Michel Deliens and Paul Piret in 1979 (Deliens and Piret, 1979c). Since their study, no additional analytical data have been reported for this phase (!). Ranunculite has a peculiar structure that contains a structural sheet of a novel topology. Along with the first structure determination from the electron diffraction, we also provide reliable Raman data and experimental powder diffraction data.

Occurrence

The specimen we used for the investigations comes from the collection of Luc Vandenberghe (Belgium) and was previously in the collection of Leopold van Wembeke, a Belgian collector who received the specimen around 1960. The specimen measures 4.4 × 3.2 × 2.8 centimeters in overall size. At the center of the specimen, there is a cavity of around 2 × 2 centimeters, which is completely filled with yellow spherical ranunculite aggregates (Fig. 1a). Isolated crystalline aggregates are also found in high relief on the matrix (Fig. 1b). These crystal aggregates form radial spheres that show a layered, finely tabular structure. The isolated crystal aggregates that reach a size of up to 0.5 millimeters (Figure 1b) are particularly suitable for further crystal structural investigations and perfectly fit the description by Deliens and Piret (1979). Notably, in this case, phuralumite, often closely associated with ranunculite, is absent on the specimen.

The ranunculite powder in the capillary used in this study has been registered as a structure type (paratype) in the Museum of Natural History in Luxembourg under the catalogue number PV038.

Ranunculite is only known with certainty from one locality, the type locality of the Kobokobo pegmatite in the Democratic Republic of Congo. We emphasize that we tried to get access to the type specimen deposited in the collections of the Royal Museum of Central Africa, Tervuren, Belgium (RGM 6201), but without success.

Raman spectroscopy

The Raman spectrum of ranunculite (Fig. 2) was collected in the range 1800–40 cm^{-1} (high-resolution settings, grating of the grid: 830 lines/mm; ~2 cm^{-1}) using a DXR dispersive Raman Spectrometer (Thermo Scientific) mounted on a confocal Olympus microscope. The Raman signal was excited by an unpolarised near-infrared 780 nm solid-state diode-pumped laser and detected by a CCD detector. The experimental parameters were: 50× objective, 2 s exposure time, 64 exposures, 50 μm slit, aperture and 8 mW laser power level. The spectra were repeatedly acquired from different grains to obtain a representative spectrum with the best signal-to-noise ratio. No thermal damage was observed by visual inspection of the excited surface after measurement, observation of possible decay of spectral features at the start of excitation, and checking for thermal downshift of Raman lines. The instrument was set up using a software-controlled calibration procedure using multiple neon emission lines (wavelength calibration), multiple polystyrene Raman bands (laser-frequency calibration), and standardized white-light sources (intensity calibration). Spectral manipulations were performed using the Omnic 9 software (Thermo Scientific). Raman spectrum of ranunculite is deposited and available as supplementary material (*.*csv* file).

The main bands observed in the Raman spectrum of ranunculite (Fig. 2) in the region between 50 and 1800 cm^{-1} are: 154, 204, 251, 327, 443, 582, 820, 1037, 1152 and 1612 cm^{-1}. To our knowledge, no Raman spectrum of natural and synthetic ranunculite has been published. The following interpretation of the ranunculite spectrum is based on the papers by Čejka (1999), Nakamoto (2009), Sejkora *et al.* (2024), and references therein. A weak band at 1612 cm^{-1} is attributed to the ν_2 bending vibrations of water molecules. A very weak band at 1152 cm^{-1} and a weak band at 1037 cm^{-1} correspond to the ν_3 $(PO_4)^{3-}$ asymmetric stretching and ν_1 $(PO_4)^{3-}$ symmetric stretching vibrations, respectively. The prominent Raman band at 820 cm^{-1} with a shoulder at 800 cm^{-1} are attributed to the ν_1 $(UO_2)^{2+}$ symmetric stretching vibrations. Using the empirical relationship of Bartlett and Cooney (1989) we have calculated corresponding approximate U–O bond lengths as 1.791 Å (820 cm^{-1}) and 1.810 Å (800 cm^{-1}), which are in line with values from the structure refinement. A weak band at 582 cm^{-1} is connected with the triply degenerate ν_4 (δ) $(PO_4)^{3-}$ bending vibrations, and a strong one at 443 cm^{-1} to the doubly degenerate ν_2 $(PO_4)^{3-}$ bending vibrations. A weak band at 251 cm^{-1} is related to the ν_2 $(UO_2)^{2+}$ doubly degenerate bending vibrations. Other observed bands, 204 and 154 cm^{-1} may be attributed to O_{eq}–U–O_{eq} bending vibrations (Ohwada, 1976), UO_2^{2+} translations and rotations, and external lattice vibration modes (Plášil *et al.*, 2010).

X-ray powder diffraction data

Powder X-ray diffraction data were collected at room temperature by Rigaku SmartLab 9 kW rotation anode diffractometer (Cu$K\alpha_{1,2}$ by curved Göbel mirror providing focused beam for Debye-Scherrer geometry) equipped with D/tex Ultra 250 detector. Ranunculite powder was loaded into a 3 mm borosilicate-glass capillary and data were collected in 20 repeating runs from 3–80° 2θ (with an integrated step size of 0.01°2θ and a variable counting time. Positions and intensities of diffractions were found and refined using the Pearson VII profile-shape function of the ZDS program package (Ondruš, 1993). The unit-cell parameters of barronite

were refined by the least-squares program of Burnham (1962). The X-ray powder diffraction pattern of ranunculite is reported in Table 2 compared to data from the original description of ranunculite (Deliens and Piret, 1979). The refined unit-cell parameters (for the space group *C*2/*c*) are a = 11.183(6) Å, b = 17.918(8) Å, c = 18.086(13) Å, β = 98.50(8)°, with V = 3584(3) Å^3 (Z = 4). The PowderCell program was used to calculate and visualize the theoretical powder pattern of ranunculite (Kraus and Nolze, 1996).

Electron crystallography

Data collection

To reveal the structure of ranunculite, we employed three-dimensional electron diffraction (3D ED) techniques using a transmission electron microscope (TEM) (Gemmi and Lanza, 2019; Gemmi *et al.*, 2019). A spherical aggregate of ranunculite crystals was gently crushed in a mortar in propanol and deposited on a Cu-grid coated with a thin film of holey amorphous carbon. To prevent dehydration caused by the TEM's high vacuum, the grid was plunged into liquid nitrogen and then transferred to the TEM using a Gatan cryo-plunging transfer holder (Mugnaioli *et al.*, 2020; Steciuk *et al.*, 2021, 2024). The 3D ED data were collected at 97K with a continuous rotation mode in an FEI Tecnai G2 TEM (acceleration voltage of 200 kV, LaB_6) equipped with a side-mounted hybrid single-electron detector ASI Cheetah M3, 512×512 pixels with high sensitivity and fast readout. For each selected crystal (Fig. 2a), a series of non-oriented patterns was continuously collected by steps of 0.3°, on all the accessible tilt ranges of the goniometer. The data collections were automated by the in-house software, including the tracking of the crystal (Plana-Ruiz *et al.*, 2018). In addition to the low-temperature experiment, low-illumination settings were used to further limit the beam-induced crystal damage. Continuous-rotation 3D ED data (cRED) reduction was performed using the computer program PETS2 (Palatinus *et al.*, 2019; Brázda *et al.*, 2022; Klar *et al.*, 2023). It includes the correction of geometrical and optical distortions to get accurate lattice parameters and better integration of the reflections (Brázda *et al.*, 2022). Three data sets were merged in PETS2 to improve the data coverage and get better statistics on lattice parameters. The quality of the merge data set is represented on the plots of the rocking curves (Camel plot) by the *rocking-curve width* as well as the estimation of the crystal mosaicity (Fig. 2b). The specific data processing for cRED data used in the structure solution and the refinement (with and without the dynamical approaches) was given by Klar *et al.* (2023). Overlapping virtual frames (*OVFs*) were produced from the tilt series of frames to model experimental intensities from continuous rotation data by summing consecutive experimental diffraction patterns into a set of virtual frames. Each *OVF* was characterized by its angular range $\Delta\alpha_v$ covered by the virtual frame and the angular step between two virtual frames (Table 3). The solution and the refinement using the kinematical approximation were based on three merged datasets (R_{int} (obs/all) = 0.3620/0.3730). The structure was solved using Superflip (Palatinus and Chapuis, 2007) implemented in Jana2020 (Petříček *et al.*, 2023) and refined using DYNGO and Jana2020. Some polyhedral measures were calculated using the Vesta program (Momma and Izumi, 2011). The Topos program (Blatov *et al.*, 2014) was used for complexity calculations.

Structure solution and refinement

According to 3D ED data, ranunculite is monoclinic with a *C*-centered cell: a = 11.1812(7) Å, b = 17.9281(5) Å, c = 17.91548(16) Å, β = 98.350(4) °, and V = 3553.2(2) Å^3. Despite the preferential (001) orientation on the grid, merging data sets allowed an increase in the data completeness to reach 85% data coverage for $\sin\theta_{max}/\lambda$ = 0.625 Å^{-1} (*Laue class*: 2/*m*). Merging data also allowed for more accurate lattice parameters and better statistics. The diffuse rows of reflections along **c** on the *h*0*l* section make the symmetry determination ambiguous. The sections of the reciprocal space suggest the possible presence of a *c*-glide perpendicular to **b** *(l = 2n on h0l).* Possible space groups were *C*2/*c*, *C*2/*m*, *C*2, *Cm*, and *P*–1 (in the primitive cell). The different symmetries and solutions were tested in the Superflip program. A complete solution describing the two dense layers was exclusively obtained in the space group *C*2/*c*. This is in line with the Superflip space-group determination (from the symmetry of the flipped electron density). The initial electrostatic potential map was re-interpreted manually based on the visible cation coordination and the result of the WDS analysis. Aluminum was placed at the center of an octahedra, a uranium atom in pentagonal or hexagonal bipyramids, and phosphorus in tetrahedral coordination. Both kinematical and dynamical approaches were tested to refine the model against 3D ED data of the first data set. Possibly, due to imperfect crystallization resulting in stacking faults along **c** (visible on the (a,c) plane), none of those approaches lead to satisfying *R*-values. However, the refined model and the topology make sense when applying cation-oxygen distance restrictions. In this study, only the kinematical refinement is presented because the dynamical theory did not yield structure improvements on the relatively poor data set and was computationally demanding. The details of the kinematical refinement are given in Table 3. Restrictions were applied to ensure reasonable cation–oxygen distances and O···O distances in some polyhedra (P–O = 1.49 Å, U–O_{yl} = 1.8 Å, Al–O = 1.9 Å). Note that lower symmetries were also tested during the refinement. However, none improved the model, indicating that the refinement limitations were due to poor data rather than incorrect space group attribution. The final model is presented in Figure 5, positional parameters and atomic displacement parameters in Table 4, and selected interatomic distances in Table 5. The limited data quality did not allow the determination of the hydrogen positions from the difference-Fourier maps. The nature of the oxygen atoms (distribution of O^{2-}, hydroxyl, or water molecules in the structure) was based on the bond-valence analysis (Table 4; using bond-valence parameters given by Gagné and Hawthorne, 2015). The resulting formula is electro-neutral, $Al_4(UO_2)_4O_2(PO_4)_4(OH)_4(H_2O)_7(H_2O)_{1.5}$ for Z = 4. The cation ratio corresponds to the original description of ranunculite as a mineral by Deliens and Piret (1979c).

Description of the structure

Based on the 3D ED data, the structure of ranunculite (Fig. 5) contains two independent U sites, two P sites, three Al sites and twenty-two O sites in the asymmetric unit (Table 4). The U1 site is coordinated by seven O atoms, two with short bonds forming a uranyl ion UO_2^{2+}, and five located at the horizontal vertices of the pentagonal uranyl bipyramid. The U2 site is linked to eight O atoms, two forming a uranyl ion UO_2^{2+}, and six located at the horizontal vertices of the hexagonal uranyl bipyramid. The U–O bond lengths were bound by the soft restrictions (see above); the refined values (see Table 5) are consistent with the most typical lengths observed for uranyl coordination polyhedra in minerals and inorganic compounds

(Lussier *et al.*, 2016). The P1 and P2 sites are coordinated as regular tetrahedra by four O atoms (none protonated as PO_3OH). The Al1 site is coordinated by six O atoms (all of them O^{2-}, based on BVS; Table 4) forming an octahedron (EcoN = 5.9998, bond-angle variance = 7.296°^2, average Al–O = 1.95 Å, expected Al–O = 1.89 Å, BVS = 2.65 *vu*). The Al2 site is coordinated by six O atoms (from them, O9 and O15 are OH^-; Table 4), also forming an octahedron (EcoN = 5.9885, bond-angle variance = 7.7037°^2, average Al–O = 1.96 Å, expected Al–O = 1.89 Å, BVS = 2.62 *vu*). The Al3 site is coordinated by five ligands (of them, O9 and O15 are OH^-; Table 4) as a tetragonal pyramid (EcoN = 4.988, average Al–O = 1.95 Å, expected Al–O = 1.82 Å, BVS = 2.23 *vu*). Based on the bond-valences analysis, the following O atoms, including O2, O4, O5, O19, O20, O21, and O22, belong to molecular H_2O (in sum, 8.5 H_2O, of which 1.5 H_2O is hosted in the voids of the structure = O21, O22; see further).

Structure connectivity and sheet topology

Two oppositely oriented pentagonal bipyramids (*UPB*, U1) form dimers of edge-sharing uranyl hexagonal bipyramids (*UHB*; U2) (Fig. 6a), resulting in a cluster of uranyl coordination polyhedra (in yellow color, Fig. 6b). Those clusters share two edges of the UHB with the octahedra of Al1 (along [100]). The Al1-octahedron shares four equatorial vertices with PO_4 tetrahedra, which in turn share one edge with UHB and one vertex with neighboring UPB. The remaining vertex of each PO_4 is not linked within the resulting sheet and is staggered into the interlayer, providing a linkage with Al2 octahedra. The Al2 octahedron is linked to the uranyl phosphate sheets by sharing three O atoms (apical $O7_{yl}$, equatorial $O8_{PO4}$, equatorial $O10_{PO4}$). The other apex (vertex) of the Al2-octahedron is the O2 atom, which points to the interlayer space of the ranunculite structure and is an H_2O group based on the BVS analysis. The remaining ligands of the Al2 octahedra are O9 and O15 atoms, belonging to the OH groups (Table 4) and linking Al2 octahedra to Al3 pyramids. The three remaining ligands of the Al3-pyramids are H_2O molecules (O5, O19, and O20).

The infinite sheets of polyhedra (structural units) are perpendicular to **c**, and adjacent sheets are linked in two ways, as some of the O atoms within the Al-polyhedra are partially occupied. Regions (unit cells) in which adjacent sheets are linked by hydrogen bonds only alternate with those where sheets are linked *via* tetramers of Al-polyhedra (through shared O19). H-bonds emanate from the H_2O groups that are of the transformer type (for terminology, see Hawthorne and Schindler, 2009; [3]-coordinated O atoms): **O2**, O5, **O19**, **O20** (in bold are those that secure interactions with adjacent sheets). The H atoms of the OH groups (donors are O9 and O15) interact either with the O atoms (acceptors) of the H_2O groups in the interlayer (O21 and O22) or with apical O_{uranyl} atoms of adjacent layers. Both O21 and O22 are non-transformer H_2O groups with [4]-coordinated O atoms (bonded to two H-atoms as H_2O and accepting two weak H-bonds, 2×0.8 *vu* + 2×0.2 *vu* = 2.00 *vu*). Hydrogen bonds emanating from the O2 atom are accepted by O21/O22 or apical O_{uranyl} atoms of adjacent layers. The alternation of regions with stronger and weaker interlayer bonding leads most probably to the statistically high distribution of stacking faults, which contributes significantly to the diffraction profiles (Fig. 4).

The uranyl-phosphate sheet in ranunculite (Fig. 6a) is a novel topological type, consisting of hexagons, pentagons, squares, and triangles (*TrSqPtHx* sheet). The ring symbol

(derived after Krivovichev, 2004) is $6^1 5^1 4^2 3^2$. In the case of ranunculite, hexagons of the topology are occupied by U^{6+} and pentagons as well; Al^{3+} populates part of the squares, and part is void. Triangles of the topology here are occupied by P^{5+}. Despite being novel, the topology found in ranunculite shares some similarities with other known, complex topologies. The bijvoetite topology (Fig. 6c) found in the structures of bijvoetite-(Y) (Li *et al.*, 2000) and kamotoite-(Y) (Plášil and Petříček, 2017) is very similar to the ranunculite topology. The main difference is that clusters of hexagons and pentagons (*HxPt*, yellow modules in Fig. 6c) are linked into infinite chains and shifted along the direction of the elongation of chains. Thus, the adjacent *HxPt* clusters are shifted to each other in bijvoetite (this corresponds to about 30° rotation of the red rectangles, Figs 6b, c). In ranunculite, *HxPt* clusters are separated by the cluster of squares and triangles (blue cluster in Figs 6b, c). In ranunculite, the central square of that cluster is occupied by Al^{3+}, while in bijvoetite, it is occupied by Y^{3+}. Triangles (blue cluster) are occupied by C^{4+} in bijvoetite. A similar *HxPt* cluster exists in the lepersonnite topology, present in the structure of lepersonnite-(Gd) (Plášil *et al.*, 2025). Nevertheless, the topology is even more complex in that case, hosting two additional infinite chains: one of pentagons and triangles and the second of hexagons and triangles (Si^{4+} populates those associated with hexagons). Bijvoetite and lepersonnite topologies contain the same arrangement of *HXPT* with triangles (green cluster in Figs 6c, d).

Stereoisomerism within ranunculite sheets

As the fourth corner of the tetrahedra in the ranunculite-type sheets is not involved in the intra-sheet polymerization of coordination polyhedra, it may thus be oriented either up or down relative to the plane of the sheet. This results in different orientational geometrical isomers (Krivovichev, 2010). Here, in the studied structure (Fig. 7a), it is the *ud* isomer, where the vertices' orientation alternates alongside the respective chain.

Kobokobo pegmatite – home of unusual uranyl minerals – a few concluding remarks

The Kobokobo pegmatite (Safiannikoff and Van Wambeke, 1967; Van Wambeke, 1987) is among the most peculiar mineralogical localities in the World. e The incorporation of Th within the otherwise U^{6+}-dominated minerals is particularly unusual. It indicates rather special conditions during the crystallization, as Th^{4+} is mobile under different conditions from U^{6+}. Recently, intriguing discoveries of rare Th^{4+}-containing minerals, two molybdates and halide minerals from the small Mo-Bi occurrence at Su Seinargiu in Sardinia, Italy (Orlandi *et al.*, 2014, 2015, 2017) have been made. However, our knowledge of the Th^{4+} behavior during alteration processes is still less understood.

In the study of Dal Bo *et al.* (2017b), it has been documented that phuralumite, $Al_2[(UO_2)_3(PO_4)_2O(OH)](OH)_3(H_2O)_9$ (Z = 4), is often closely associated with ranunculite. Usually, phuralumite crystals grow on the underlying globular aggregates of ranunculite. Interestingly, the ranunculite formula derived from our study is $Al_4(UO_2)_4O_2(PO_4)_4(OH)_4(H_2O)_7(H_2O)_{1.5}$ (Z = 4). These two minerals have very similar densities (Table 6) and molecular H_2O content. This resembles the case of stable and metastable polymorphs. Krivovichev (2017) demonstrated for polymorphic minerals, gilmarite and clinoclase, that the metastable phase (gilmarite), which is structurally simpler than the stable one (clinoclase), crystallized prior to the stable phase under some kinetically

favored conditions. He also demonstrated that according to the Ostwald–Volmer rule (Holleman *et al.*, 2001), for metastable crystallization, the less dense metastable phase forms first because, under supersaturated conditions, its nuclei reach their critical sizes faster than those of the stable phase (Fischer and Jansen, 2002; Bach *et al.*, 2013). Although ranunculite and phurcalite are not polymorphs (as phuralumite is based upon phosphuranylite topology), their proximity in chemistry, density, and other properties is worth investigating and discussing further. Ranunculite is a much simpler phase from the point of view of the structural complexity concept (Krivovichev, 2012, 2013, 2016) (Table 6). From all the observed features of the structure and properties of ranunculite, we can conclude that the structure of ranunculite can be considered as less ordered compared to that of phuralumite; ranunculite contains many stacking faults (manifested in the powder diffraction data by the presence of anisotropic broadening); ranunculite crystallizes, in contrast to phuralumite, in minute crystals in radial aggregates. This noticeable difference in appearance suggests that ranunculite is most probably the result of quick crystallization from the saturated/oversaturated solutions. After that, crystallization of a more ordered, more structurally complex phase – phuralumite proceeds.

It is worth considering the structural complexities of some other actinoid-bearing mineral species from Kobokobo. The calculated structural and chemical complexity measures are reported in Table 7 and are displayed for comparison in Figure 7. The chemical complexity (after Siidra *et al.*, 2014) is estimated by considering the chemical formula as a message, where symbols correspond to different chemical elements. Interestingly, ranunculite has very similar figures (both structurally and chemically) as kamitugaite, another very peculiar phase from Kobokobo (the only phase in that system containing Pb^{2+} and As^{5+}). Phuralumite, which is often associated with ranunculite (never associated with kamitugaite and vice versa), is more complex structurally and less so chemically. Furongite, althupite, and phosphuranylite are structurally and chemically complex minerals, reaching the highest values within the given mineral system. In general, they are also very stable alteration phases formed from primary U minerals (see Krivovichev and Plášil, 2013; Plášil, 2014). This is probably in line with the fact that they are the most complex in the given mineral system (the most stable ones = with the highest complexity).

Acknowledgments

The helpful comments of two anonymous reviewers, as well as editors, are greatly appreciated. This study was supported by the CzechNanoLab Research Infrastructure supported by MEYS CR (LM2023051). Additionally, we acknowledge the support by the Ministry of Culture of the Czech Republic (long-term project DKRVO 2024-2028/1.II.b; National Museum, 00023272) for JS.

References

Bach, A., Fischer, D., and Jansen, M. (2013) Metastable phase formation of indium monochloride from an amorphous feedstock. *Zeitschrift für Anorganische und Allgemaine Chemie*, **639**, 465–467.

Bartlett J.R. and Cooney R.P. (1989) On the determination of uranium-oxygen bond lengths in dioxouranium(VI) compounds by Raman spectroscopy. *Journal of Molecular Structure*, **193**, 295–300.

Blatov, V.A., Shevchenko, A.P. and Proserpio, D.M. (2014) Applied topological analysis of crystal structures with the program package ToposPro. *Crystal Growth & Design*, **14**, 3576–3586.

Brázda P., Klementová, M., Krysiak, Y., and Palatinus, L. (2022) Accurate lattice parameters from 3D electron diffraction data. I. Optical distortions. *International Union of Crystallography Journal*, **9**, 1–21.

Burnham C. W. (1962) Lattice constant refinement. *Carnegie Institute Washington Yearbook*, **61**, 132–135.

Čejka J. (1999) Infrared spectroscopy and thermal analysis of the uranyl minerals. *Reviews in Mineralogy*, **38**, 521–622.

Chakoumakos, B. C., Abraham, M. M. and Boatner, L. A. (1994) Crystal structure refinements of zircon-type MVO_4 (*M* = Sc, Y, Ce, Pr, Nd, Tb, Ho, Er, Tm, Yb, Lu). *Journal of Solid State Chemistry*, **109**, 197–202.

Dal Bo, F., Hatért, F. and Philippo, S. (2017a) A new uranyl phosphate sheet in the crystal structure of furongite. *European Journal of Mineralogy*, **29**: 517–527.

Dal Bo, F., Hatért, F., Philippo, S. (2017b) New crystallographic data and formula revision of phuralumite, $Al_2[(UO_2)_3(PO_4)_2O(OH)](OH)_3(H_2O)_9$. *Journal of Geosciences*, **62**, 87–95.

Deliens, M., Piret, P. (1979a) Les phosphates d'ura nyle et d'aluminium de Kobokobo. II. La phuralumite $Al_2(UO_2)_3(PO_4)_2(OH)_6{\cdot}10H_2O$ et l'upalite $Al(UO_2)_3(PO_4)_2(OH)_3$, nouveaux minéraux. *Bulletin de Minéralogie*, **10**2: 333–337.

Deliens, M. and Piret, P. (1979b) Les phosphates d'uranyle et d'aluminium de Kobokobo. IV. La threadgoldite, $Al(UO_2)_2(PO_4)_2(OH){\cdot}8H_2O$, nouveau minéral. *Bulletin de Minéralogie*, **102**, 338–341.

Deliens M. and Piret P. (1979c) Ranunculite, $AlH(UO_2)(PO_4)(OH)_3{\cdot}4H_2O$, a new mineral. *Mineralogical Magazine*, **43**, 321–323.

Deliens, M. and Piret, P. (1981) Les phosphates d'uranyle et d'aluminium de Kobokobo. V. La mundite, nouveau minéral. *Bulletin de Minéralogie*, **104**, 669–671.

Deliens, M. and Piret, P. (1982) Les phosphates d'uranyle et d'aluminium de Kobokobo. VI. La triangulite, $Al_3(UO_2{\cdot}PO_4)_4(OH)_5{\cdot}5H_2O$, nouveau minéral. *Bulletin de Minéralogie*, **105**, 611–614.

Deliens, M. and Piret, P. (1984) La kamitugaïte, $PbAl(UO_2)_5[(P,As)O_4]_2(OH)_9{\cdot}9{,}5H_2O$, nouveau minéral de Kobokobo, Kivu, Zaïre. *Bulletin de Minéralogie*, **107**: 15–19.

Deliens, M. and Piret, P. (1985a) Les phosphates d'uranyle et d'aluminium de Kobokobo. VII. La moreauïte, $Al_3UO_2(PO_4)_3(OH)_2\ {\cdot}13H_2O$, nouveau minéral. *Bulletin de Minéralogie*, **108**, 9–13.

Deliens, M. and Piret, P. (1985b) Les minéralisations secon daires d'uranium associées à la pegmatite de Kobokobo, Kivu, Zaire. Revue des phosphates d'uranium du groupe structural de la phosphuranylite–dumontite. Rapp a Dép Géol Minéral Mus roy Afr cent, Ann 1983–1984, pp 81–86.

Deliens, M. and Piret, P. (1986) La kusuïte devient la wakefïeldite-(Ce) plombifère. *Bulletin de Minéralogie*, **109** (3) 305.

Fischer, D. and Jansen, M. (2002) Low-activation and solid-state syntheses by reducing transport lengths to atomic scales as demonstrated by case studies on $AgNO_3$ and AgO. *Journal of American Chemical Society*, **124**, 3488–3489.

Gagné, O.C. and Hawthorne, F.C (2015) Comprehensive derivation of bond-valence parameters for ion pairs involving oxygen. *Acta Crystallographica*, **B71**, 562–578.

Gemmi M. and Lanza A.E. (2019) 3D electron diffraction techniques. *Acta Crystallographica Section B: Structural Science, Crystal Engineering and Materials*, **75**, 495–504.

Gemmi M., Mugnaioli E., Gorelik T.E., Kolb U., Palatinus L., Boullay P., Hovmöller S. and Abrahams J.P. (2019) 3D electron diffraction: The nanocrystallography revolution. *ACS Central Science*, **5**, 1315–1329.

Hawthorne, F.C. and Schindler, M. (2009) Understanding the weakly bonded constituents in oxysalt minerals. *Zeitschrift für Kristallographie - Crystalline Materials*, **223**, 41–68.

Holleman, A.F., Wiberg, F. and Wiberg, N. (2001) Inorganic Chemistry. Academic Press, San Diego, CA, pp 1–507.

Hunan 230 Laboratory, Hunan 305 Geological Team and X-ray Laboratory, Wuhan Geological Institute (1976) Furongite - a new uranium mineral found in China. *Acta Geologica Sinica*, **2**, 203–204.

Khosrawan-Sazedj, F. (1982) On the space group of threadgoldite. *Tschermaks Mineralogische und Petrographische Mitteilungen*, **30**, 111–115.

Klar, P.B., Krysiak, Y., Xu, H., Steciuk, G., Cho, J., Zou, X., Palatinus, L. (2023) Accurate structure models and absolute configuration determination using dynamical effects in continuous-rotation 3D ED data. *Nature Chemistry*, **15**, 1–8.

Krivovichev, S.V. (2004) Combinatorial topology of salts of inorganic oxoacids: zero-, one- and two-dimensional units with corner-sharing between coordination polyhedra. *Crystallography Reviews*, **10**, 185–232.

Krivovichev, S.V. (2010) Actinyl compounds with hexavalent elements (S, Cr, Se, Mo) - structural diversity, nanoscale chemistry, and cellular automata modelling. *European Journal of Inorganic Chemistry*, **2010**, 2594–2603.

Krivovichev, S.V. (2012) Topological complexity of crystal structures: quantitative approach. *Acta Crystallographica*, **A68**, 393–398.

Krivovichev, S.V. (2013) Structural complexity of minerals: information storage and processing in the mineral world. *Mineralogical Magazine*, **77**, 275–326.

Krivovichev, S.V. (2016) Structural complexity and configurational entropy of crystals. *Acta Crystallographica*, **B72**, 274–276.

Krivovichev, S.V. (2017) Hydrogen bonding and structural complexity of the $Cu_3(AsO_4)(OH)_3$ polymorphs (clinoclase, gilmarite): a theoretical study. *Journal of Geosciences*, **62**, 79–85.

Krivovichev, S.V. and Plášil, J. (2013) Mineralogy and crystallography of uranium. in "Uranium, from cradle to grave", P.C. Burns and G.E. Sigmon, eds. MAC. Short Course, 43, pp. 15–119, Winnipeg MB, May 2013.

Li, Y., Burns, P.C. and Gault, R.A. (2000) A new rare-earth element uranyl carbonate sheet in the structure of bijvoetite-(Y). *The Canadian Mineralogist*, **38**, 153–162.

Lussier, A. J., Lopez, R. A. and Burns, P. C. (2016) A revised and expanded structure hierarchy of natural and synthetic hexavalent uranium compounds. *The Canadian Mineralogist*, **54**, 177–283.

Mills, S.J., Birch, W.D., Kampf, A.R. and van Wambeke, L. (2010) Kobokoboite, $Al_6(PO_4)_4(OH)_6 \cdot 11H_2O$, a new mineral from the Kobokobo pegmatite, Democratic Republic of the Congo. *European Journal of Mineralogy*, **22**, 305–308.

Momma, K. and Izumi, F. (2011) VESTA 3 for three-dimensional visualization of crystal, volumetric and morphology data. *Journal of Applied Crystallography*, **44**, 1272–1276.

Mugnaioli, E., Lanza, A.E., Bortolozzi, G., Righi, L., Merlini, M., Cappello, V., Marini, L., Athanassiou, A., and Gemmi, M. (2020) Electron Diffraction on Flash-Frozen Cowlesite Reveals the Structure of the First Two-Dimensional Natural Zeolite. *ACS Central Science*, **6**, 1578–1586.

Nakamoto K. (2009) *Infrared and Raman spectra of inorganic and coordination compounds Part A: Theory and applications in inorganic chemistry*. John Wiley and Sons Inc. Hoboken, New Jersey.

Ohwada K. (1976) Infrared spectroscopic studies of some uranyl nitrate complexes. *Journal of Coordination Chemistry*, **6**, 75–80.

Ondruš P. (1993) A computer program for analysis of X-ray powder diffraction patterns. *Materials Science Forum, EPDIC-2, Enchede*, 133-136, 297-300.

Orlandi, P., Biagioni, C., Bindi, L. and Nestola, F. (2014) Ichnusaite, $Th(MoO_4)_2 \cdot 3H_2O$, the first natural thorium molybdate: occurrence, description, and crystal structure. *American Mineralogist*, **99**, 2089–2094.

Orlandi, P., Biagioni, C., Bindi, L. and Merlino, S. (2015) Nuragheite, $Th(MoO_4)_2 \cdot H_2O$, the second natural thorium molybdate and its relationships to ichnusaite and synthetic $Th(MoO_4)_2$. *American Mineralogist*, **100**, 267–273.

Orlandi, P., Biagioni, C. and Zaccarini, F. (2017) Cabvinite, $Th_2F_7(OH) \cdot 3H_2O$, the first natural actinide halide. *American Mineralogist*, **102**, 1384–1389.

Palatinus L. and Chapuis G. (2007) SUPERFLIP—a computer program for the solution of crystal structures by charge flipping in arbitrary dimensions. *Journal of Applied Crystallography*, **40**, 786–790.

Palatinus L., Brázda P., Jelínek M., Hrdá J., Steciuk G., and Klementová M. (2019) Specifics of the data processing of precession electron diffraction tomography data and their implementation in the program PETS2.0. *Acta Crystallographica*, **B75**, 512–522.

Petříček, V., Dušek, M., Plášil, J. and Palatinus, L. (2023) Jana2020 - a new version of the crystallographic computing system Jana. *Zeitschrift für Kristallographie*, **229**, 345–352.

Piret, P. and Declercq, J. P. (1983) Structure cristalline de l'upalite $Al[(UO_2)_3O(OH)(PO_4)_2] \cdot 7H_2O$. Un exemple de macle mimétique. *Bulletin de Minéralogie*, **106**, 383–389.

Piret, P. and Deliens, M. (1987) Les phosphates d'uranyle et d'aluminium de Kobokobo IX. L'althupite $AlTh(UO_2)[(UO_2)_3O(OH)(PO_4)_2]_2(OH)_3 \cdot 15H_2O$, nouveau minéral; propriétés et structure cristalline. *Bulletin de Minéralogie*, **110**, 65–72.

Piret, P. and Deliens, M. (1982) La vanmeerscheite $U(UO_2)_3(PO_4)_2(OH)_6 \cdot 4(H_2O)$ et la méta-vanmeerscheite $U(UO_2)_3(PO_4)_2(OH)_6 \cdot 2(H_2O)$, nouveaux minéraux. *Bulletin de Minéralogie*, **105**, 125–128.

Plana-Ruiz, S., Portillo, J., Estradé, S., Peiró, F., Nicolopoulos, S. and Kolb, U. (2018) Quasi-parallel precession diffraction: Alignment method for scanning transmission electron microscopes. *Ultramicroscopy*, **193**, 39–51.

Plášil, J. (2014) Oxidation-hydration weathering of uraninite: The current state of knowledge. *Journal of Geosciences*, **59**, 99–114.

Plášil, J. (2017) A novel sheet topology in the structure of kamitugaite, $PbAl[(UO_2)_5(PO_4)_{2.38}(AsO_4)_{0.62}O_2(OH)_2](H_2O)_{11.5}$. *Journal of Geosciences*, **62**, 253–260.

Plášil, J. and Petříček, V. (2017) Crystal structure of the (REE)-uranyl carbonate mineral kamotoite-(Y). *Mineralogical Magazine*, **81**, 653–660.

Plášil, J., Buixaderas, E., Čejka, J., Sejkora, J., Jehlička, J. and Novák, M. (2010) Raman spectroscopic study of the uranyl sulphate mineral zippeite: low wavenumber and U–O stretching regions. *Analytical and Bioanalytical Chemistry*, **397**, 2703–2715.

Plášil, J, Steciuk, G., Sejkora, J., Kampf, A.R., Uher, P., Ondrejka, M., Škoda, R., Dolníček, Z., Philippo, S., Guennou, M., Meisser, N., Rohlíček, J. and Mees, F. (2025) Extending the mineralogy of U^{6+} (I.): Crystal structure of lepersonnite-(Gd) and a description of the new mineral lepersonnite-(Nd). *Mineralogical Magazine*, (*accepted manuscript*).

Safiannikoff, A. and Van Wambeke, L. (1967) La pegmatite radioactive à béryl de Kobokobo et les autres venues pegmatitiques et filoniennes de la région de Kamituga – Kivu – Rép. du Congo. *Mineralia Deposita*, **2**, 119–130.

Sejkora J., Kristek J., Škácha P. and Dolníček Z. (2024) Uramphite from the Nová Ves pod Pleší (Czech Republic), the third world occurrence-description and vibrational spectroscopy. *Journal of Geosciences*, **69**, 173–182.

Siidra, O., Zenko, D.S. and Krivovichev, S.V. (2014) Structural complexity of lead silicates: crystal structure of $Pb_{21}[Si_7O_{22}]_2[Si_4O_{13}]$ and its comparison to hyttsjöite. *American Mineralogist*, **99**, 817–823.

Steciuk G., Sejkora J., Čejka J., Plášil J. and Hloušek J. (2021) Krupičkaite, $Cu_6[AsO_3(OH)]_6{\cdot}8H_2O$, a new copper arsenate mineral from Jáchymov (Czech Republic). *Journal of Geosciences*, **66**, 37–50.

Steciuk G., Majzlan J., Rohlíček J., Škoda R., Sejkora J. and Plášil, J. (2024) Znucalite, the only known zinc uranyl carbonate: its crystal structure and environmental implications. *American Mineralogist*, **109**, 949–959.

Van Wambeke, L. (1972) Eylettersite, un nouveau phosphate de thorium appartenant à la série de la crandallite. *Bulletin de la Société Francaise de Minéralogie et de Cristallographie*, **95**: 98–105.

Van Wambeke, L. (1987) La minéralogie de la pegmatite de Kobokobo, Kivu, Zaïre. *Bulletin de la Societe belge de Géologie*, **96**, 137–142.

FIGURE CAPTIONS

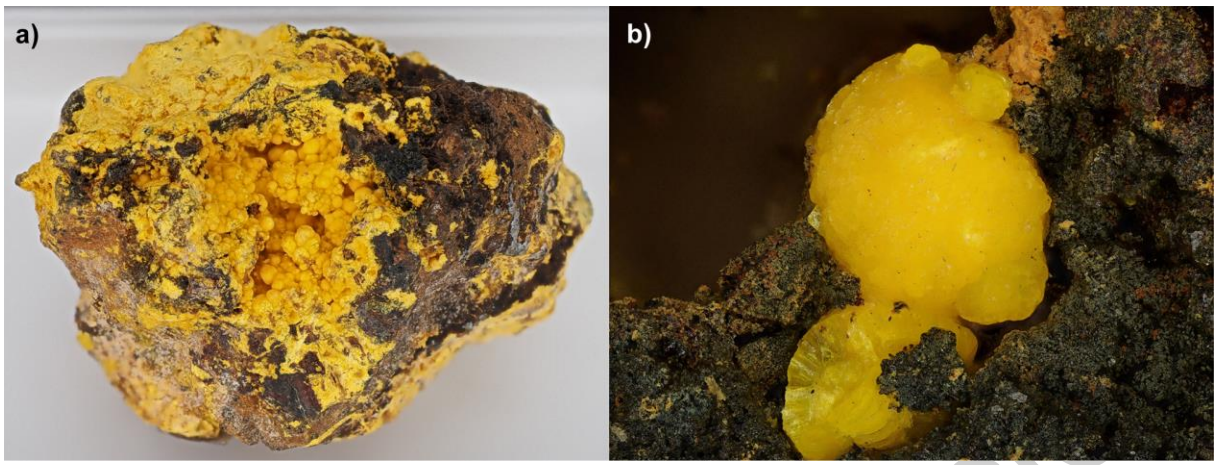

Figure 1. The ranunculite specimen from Kobokobo investigated in this study. **A)** The entire specimen (~4.4 cm across) i with a large cavity filled with ranunculite. **B)** Detail (FOV 1.5 mm) of the ranunculite aggregate studied by 3D ED and other methods (photo by A. Matthies)**.**

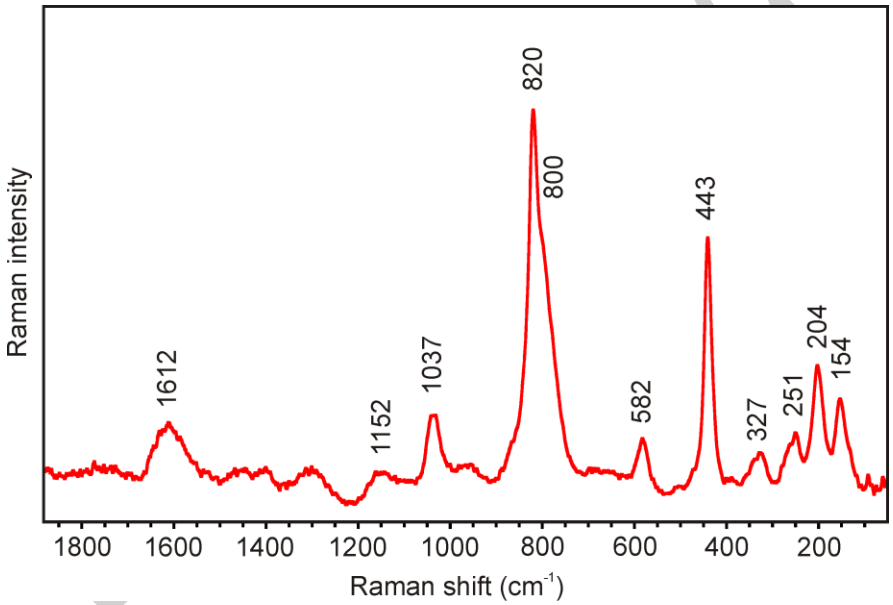

Figure 2. Raman spectrum of ranunculite measured with a 780 nm laser.

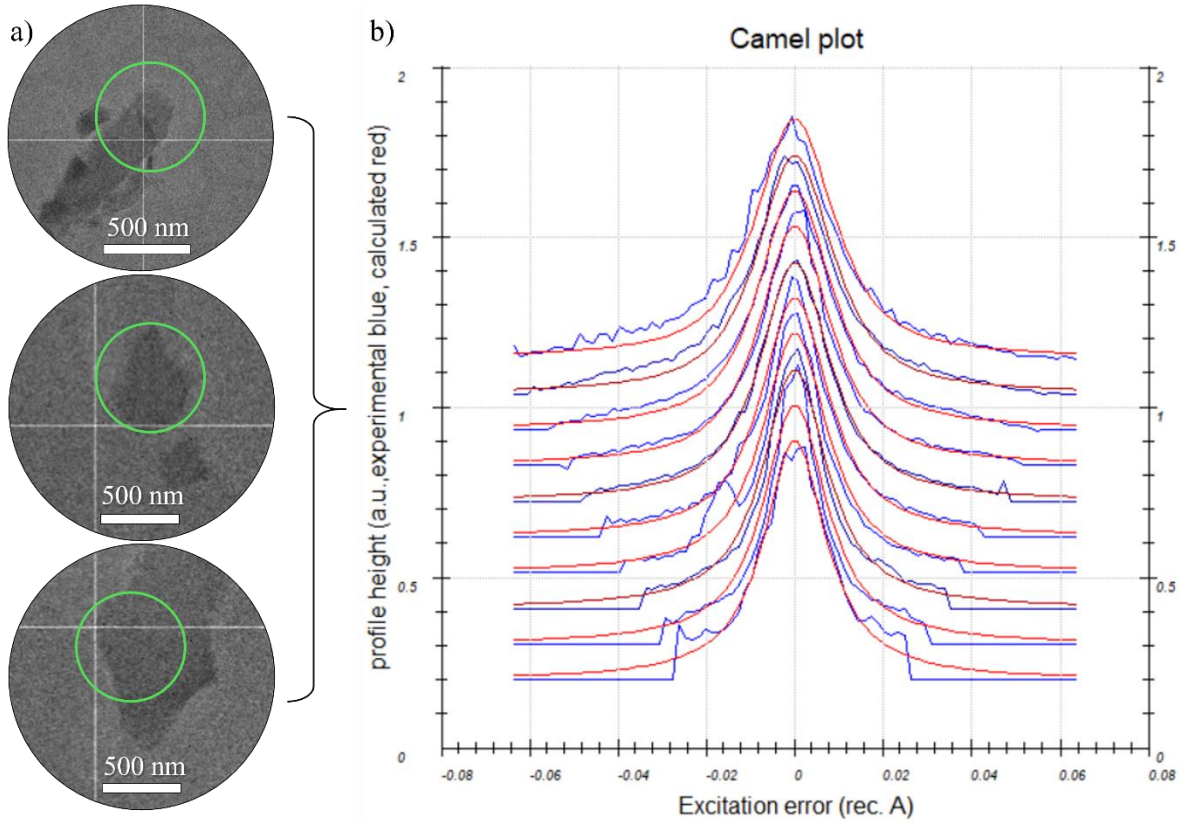

Figure 3. A) Three crystals that were used for the structure characterization by 3D ED. **B)** Rocking curve plot of the merged data. Plots of the rocking-curve profiles (Camel plot) of the experimental 3D ED merged data. The lowest blue curve is the average observed rocking curve in the range of 0.2 to 0.3 $Å^{-1}$, and the next ones are obtained by steps of 0.1 $Å^{-1}$. The red dotted curves are calculated from the *rocking curve width* = 0.0118 $Å^{-1}$, the *apparent mosaicity* = 0.197 °, and the tilt *semi-angle* = 0.15 °. $I > 10*\sigma(I)$ reflections are involved in the Camel plot.

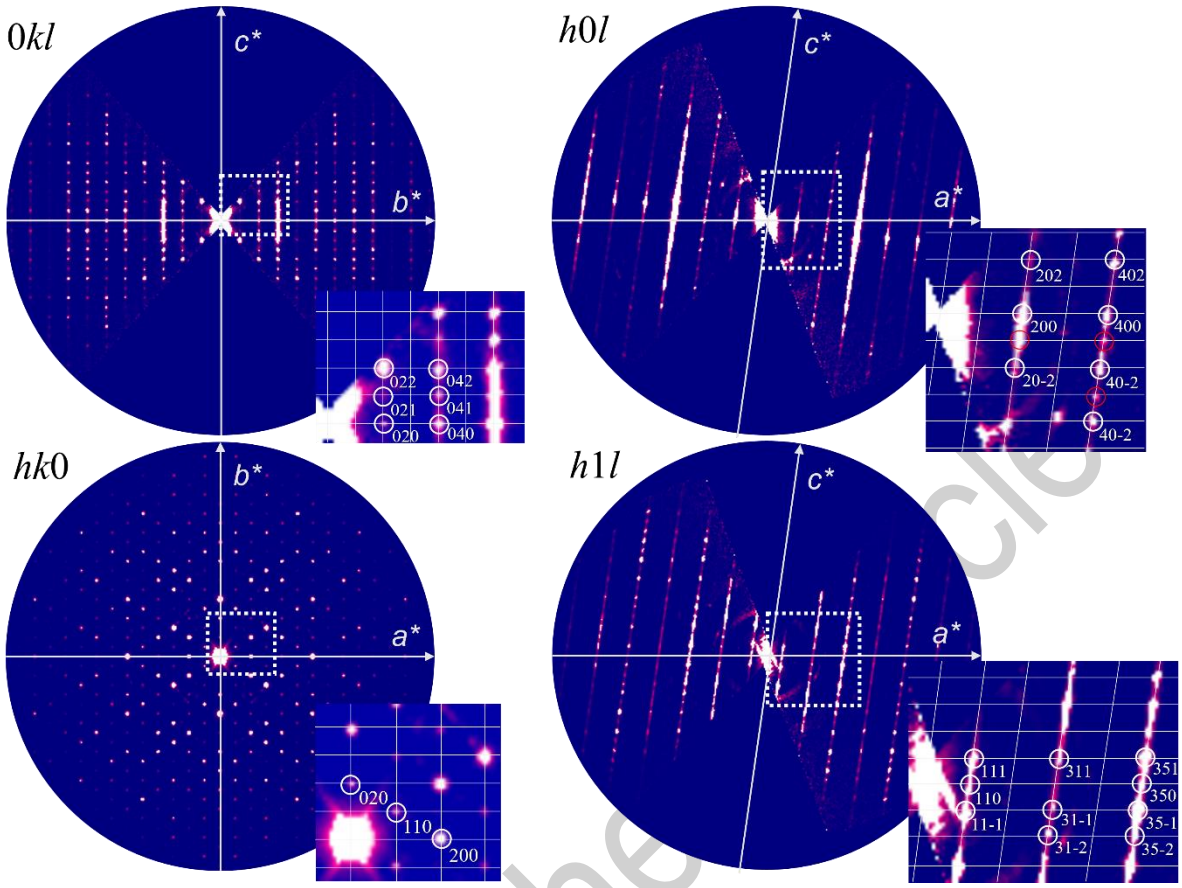

Figure 4. 0*kl*, *h*0*l*, *h*1*l*, and *hk*0 sections of the reciprocal space reconstructed from the merged data set. Red reflections are forbidden due to the **c**-glide mirror.

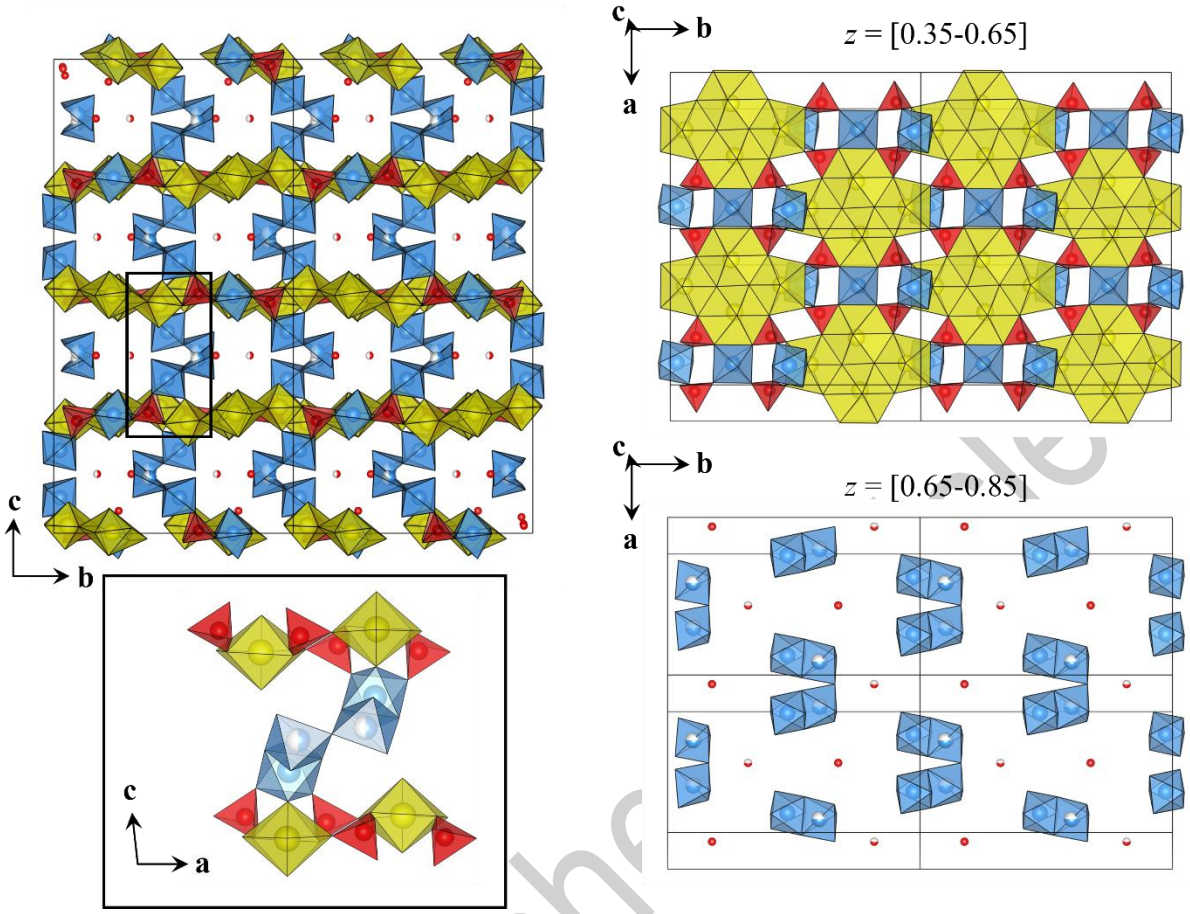

Figure 5. Crystal structure of ranunculite (represented approximately as $2a \times 2b \times 2c$ along the main directions. The uranyl-phosphate sheet is shown between $0.35 < z < 0.65$, and the Al dimers are found in the interlayers for $0.65 < z < 0.85$. Color scheme: U – yellow, PO_4 – red, Al-polyhedra blue, O atoms of the H_2O molecules – red spheres.

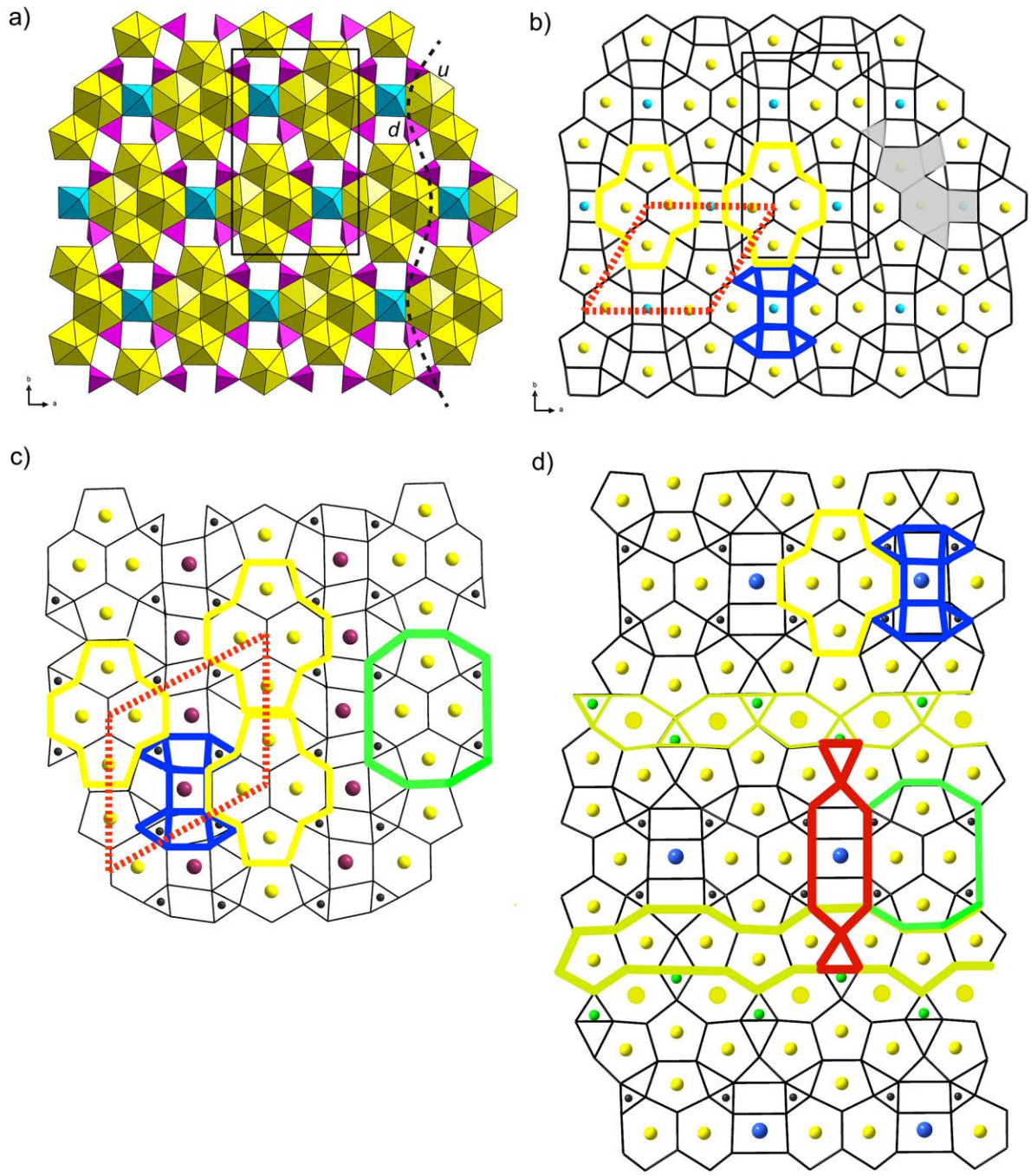

Figure 6. The uranyl-phosphate sheet present in the ranunculite structure. **A)** Detailed view of the polyhedral representation of the sheet. The color scheme for polyhedra: U – yellow, P – purple, Al – azure. The dashed line outlines the PO_4 tetrahedra and the orientation of their vertices concerning possible orientational stereoisomerism (here *ud* stereoisomer). **B)** the graph representation of its topology. Color scheme: *HxPt* cluster – yellow; *SqTr* cluster – blue; red dotted line connects the idealized centers of *HxPt* clusters. **C)** Bijvoetite topology. The color scheme is similar to the previous graph; the green border outlines the *HxPtTr* cluster, which is common with **d)** lepersonnite topology, where additional infinite chains of polyhedra are present (two types of yellow borders outlining *HxTr* chain and *PtTr* chain).

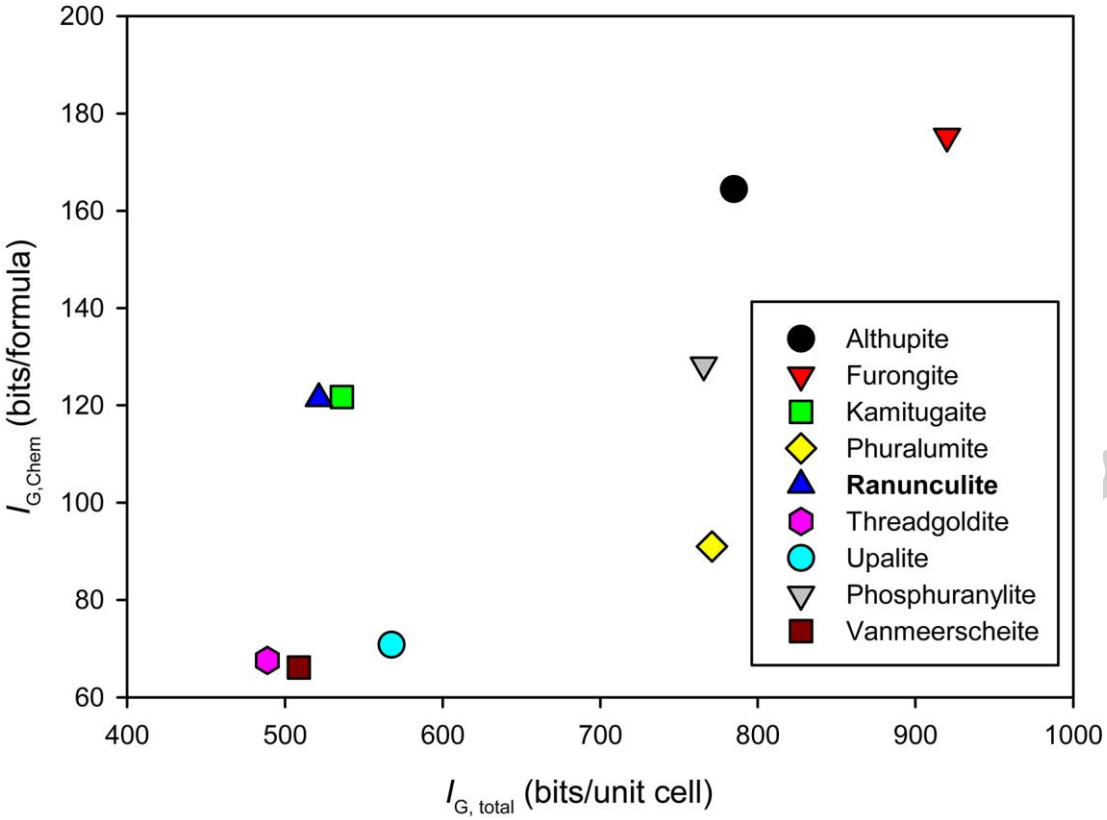

Figure 7. Complexity measures (structural *vs.* chemical) plot for actinoid-bearing phases from Kobokobo pegmatite.

Table 1. Actinoide-bearing minerals and associated type minerals discovered from the Kokobobo pegmatite, Kivu Province, Democratic Republic of Congo.

	Chemical formula	Structure determined	Primary reference
U^{6+} minerals			
Kamitugaite	$PbAl[(UO_2)_5(PO_4)_3O_2(OH)_2](H_2O)_{11}$	Plášil (2017)	Deliens and Piret (1984)
Metavanmeersscheite	$U^{6+}(UO_2)_3(PO_4)_2(OH)_6(H_2O)_2$		Piret and Deliens (1982)
Moreauite	$Al_3(UO_2)(PO_4)_3(OH)_2(H_2O)_{13}$		Deliens and Piret (1985a)
Mundite	$Al(UO_2)_3(PO_4)_2(OH)_3(H_2O)_{5.5}$		Deliens and Piret (1981)
Phuralumite	$Al_2[(UO_2)_3(PO_4)_2O(OH)](OH)_3 \cdot 9H_2O$	Dal Bo et al. (2017a)	Deliens and Piret (1979a)
Ranunculite	**$Al(UO_2)(PO_3OH)(OH)_3(H_2O)_4$**	**This paper**	**Deliens and Piret (1979c)**
Threadgoldite	$Al(UO_2)_2(PO_4)(OH)(H_2O)_8$	Khosrawan-Sazedj (1982)	Deliens and Piret (1979b)
Triangulite	$Al_3(UO_2)_4(PO_4)_4(OH)_5(H_2O)_5$		Deliens and Piret (1982)
Upalite	$Al[(UO_2)_3(PO_4)_2O(OH)](H_2O)_7$	Piret and Declercq (1983)	Deliens and Piret (1979a)
Vanmeerscheite	$U^{6+}(UO_2)_3(PO_4)_2(OH)_6(H_2O)_4$	Piret and Deliens (1982)	Piret and Deliens (1982)
Furongite*	$Al_4[(UO_2)_4(PO_4)_6](OH)_2(H_2O)_{19.5}$	Dal Bo et al. (2017b)	Hunan Team (1976)
Th-containing minerals			
Althupite	$AlTh(UO_2)_7(PO_4)_4O_2(OH)_5(H_2O)_{15}$	Piret and Deliens (1987)	Piret and Deliens (1987)
Eylettersite	$Th_{0.75}Al_3(PO_4)_2(OH)_6$		Van Wambeke (1972)
Associated type-minerals			
Wakefieldite-(Ce)	$CeVO_4$	Chakoumakos *et al.* (1994)	Deliens and Piret (1986)
Kobokoboite	$Al_6(PO_4)_4(OH)_6 \cdot 11H_2O$		Mills *et al.* (2010)

*originally described from Hunan province, China; from Kobokobo reported by Deliens and Piret (1985b).

Table 2. Powder X-ray diffraction data for ranunculite from Kobokobo.

$I_{obs.}$	$d_{obs.}$	$d_{calc.}$	h	k	l	$I_{obs.}$*	$d_{obs.}$*
100	8.923	8.944	0	0	2	100	9.00
12	8.763	8.797	-1	1	1		
1	6.340	6.329	0	2	2	3	6.37
						5	5.87
2	5.538	5.530	2	0	0	5	5.52
25	4.729	4.706	2	2	0	50	4.70
14	4.470	4.472	0	0	4	30	4.45
						10	4.02
2	3.646	3.643	-3	1	1		
3	3.577	3.581	0	4	3	20	3.53
10	3.370	3.377	-1	5	1	20	3.34
2	3.310	3.321	1	5	1		
40	3.159	3.158	-3	3	1	80	3.133
4	3.029	3.026	3	3	1		
17	2.985	2.986	0	6	0	40	2.978
		2.981	0	0	6		
						5	2.828
6	2.642	2.643	3	3	3	20	2.629
2	2.551	2.548	-1	1	7	15	2.529
1	2.3533	2.3445	2	6	3		
5	2.2183	2.2196	0	4	7	10	2.207
5	2.1087	2.1089	-3	7	1	5	2.098
3	2.0738	2.0759	2	8	0		
1	2.0464	2.0473	-2	8	2	5	2.055
2	1.9863	1.9876	-4	6	3		
2	1.9365	1.9325	3	7	3	5	1.928
4	1.8960	1.8969	-5	5	1	3	1.883
8	1.8607	1.8605	-6	0	2	40	1.850
5	1.7480	1.7494	3	7	5	10	1.741
1	1.6848	1.6830	-6	0	6		
7	1.5767	1.5791	-6	6	2	15	1.573
1	1.4564	1.4549	1	9	8		
1	1.3800	1.3811	-8	2	2		
1	1.3633	1.3618	1	13	1		
1	1.3131	1.3143	3	5	11		
4	1.2881	1.2892	0	12	7		
5	1.2134	1.2128	-9	3	1		

$I_{obs.}$*, $d_{obs.}$* - ranunculite from Kobokobo, 114.6 mm camera, Cu$K\alpha$ radiation, Ni filter (Deliens and Piret, 1979c).

Table 3. 3D ED data collection and structure refinement details for ranunculite.

Refined structural formula (with H)	$Al_4(H_2O)_7[(UO_2)_4O_2(PO_4)_4(OH)_4](H_2O)_{1.5}$
a [Å]	11.1812(7)
b [Å]	17.9281(5)
c [Å]	17.91548(16)
β [°]	98.350(4)
V [$Å^3$]	3553.2(2)
Z	4
Density [$g \cdot cm^{-3}$] (with theor. H atoms)	3.4042
Space group	*C2/c*
Temperature	97 K
TEM	FEI Tecnai G2 20
Radiation (wavelength)	electrons (0.0251 Å)
Δ*α*/total *α*-tilt (°)	data 1: 0.3/120 data 2: 0.3/120 data 3: 0.3/117
Resolution range (θ) (merged)	0.048–1.066
Limiting Miller indices	*h*: –13→ 13, *k*: 0→22, *l*: 0 → 18
No. of independent reflections (obs/all) – kinematic (merged data)	1787/3087
R_{int} (obs/all) – kinematic	0.3620/0.3730
Redundancy	3.549
Coverage for $\sin\theta_{max}/\lambda = 0.625$ $Å^{-1}$ (merged data)	85%
CC1/2 for $\sin\theta_{full}/\lambda = 0.625$ $Å^{-1}$ (merged data)	94.12%
Kinematical refinement of 3D ED data (merge data)	
No. of reflections (obs/all)	1695/2766
|F(obs)-F(calc)|>14σ(F(obs))	26 rejected reflections
R, *wR* (obs)	0.4114/0.5039
R, *wR* (all)	0.4769/0.5177
GOF(obs), GOF(all)	0.0563/0.0461
N refined param.	82

Table 4. Atom coordinates, displacement (in Å^2), occupational parameters, and bond-valence sums (in valence units) for the ranunculite structure obtained from 3D electron diffraction.

Atom	*Wyck.*	*x*	*y*	*z*	*Occ.*	U_{iso}	BVS	Assign.
U1	8*f*	0.2456(4)	0.0579(2)	0.4677(5)	1	0.0083(16)	6.19(9)	U^{6+}
U2	8*f*	0.0812(4)	0.2431(3)	0.4954(5)	1	0.0083(16)	5.69(12)	U^{6+}
P1	8*f*	0.4227(12)	0.8962(9)	0.5124(13)	1	0.027(4)	5.2(2)	P^{5+}
P2	8*f*	0.9203(11)	0.0971(9)	0.4745(13)	1	0.027(4)	5.2(2)	P^{5+}
Al1	4*c*	0.25	0.75	0.5	1	0.027(4)	2.65(7)	Al^{3+}
Al2	8*f*	0.2941(18)	0.9744(13)	0.6500(17)	1	0.027(4)	2.62(11)	Al^{3+}
Al3	8*f*	0.353(2)	0.1018(18)	0.733(2)	0.5	0.027(4)	2.23(10)	Al^{3+}
O1	8*f*	0.035(4)	0.234(3)	0.3954(7)	1	0.083(6)	1.70(6)	O^{2-}
O2	8*f*	0.320(4)	0.908(3)	0.736(2)	1	0.083(6)	0.46(6)	H_2O
O3	8*f*	0.081(5)	0.229(4)	0.5948(8)	1	0.083(6)	1.69(8)	O^{2-}
O4	8*f*	0.206(5)	0.731(3)	0.3921(9)	1	0.083(6)	0.44(2)	H_2O
O5	8*f*	0.301(4)	0.170(2)	0.650(3)	0.5	0.083(6)	0.46(3)	H_2O
O6	8*f*	0.225(3)	0.061(2)	0.3666(5)	1	0.083(6)	1.70(4)	O^{2-}
O7	8*f*	0.271(3)	0.0470(18)	0.5683(6)	1	0.083(6)	2.16(6)	O^{2-}
O8	8*f*	0.857(2)	0.0749(18)	0.3964(15)	1	0.083(6)	1.69(11)	O^{2-}
O9	8*f*	0.444(2)	0.0301(18)	0.684(3)	1	0.083(6)	0.89(5)	OH^-
O10	8*f*	0.381(3)	0.9092(18)	0.5885(15)	1	0.083(6)	1.73(13)	O^{2-}
O11	8*f*	0.870(2)	0.1711(15)	0.497(2)	1	0.083(6)	1.99(12)	O^{2-}
O12	8*f*	0.368(3)	0.8241(14)	0.4782(17)	1	0.083(6)	1.96(11)	O^{2-}
O13	8*f*	0.4402(12)	0.1096(17)	0.477(2)	1	0.083(6)	2.07(7)	O^{2-}
O14	8*f*	0.248(3)	0.1854(7)	0.469(2)	1	0.083(6)	1.84(5)	O^{2-}
O15	8*f*	0.204(2)	0.043(2)	0.706(3)	1	0.083(6)	0.86(6)	OH^-
O16	8*f*	0.382(3)	0.9609(14)	0.4600(19)	1	0.083(6)	1.84(11)	O^{2-}
O17	8*f*	0.0550(12)	0.1049(16)	0.4724(18)	1	0.083(6)	2.25(7)	O^{2-}
O18	8*f*	0.101(3)	0.9629(17)	0.4683(17)	1	0.083(6)	1.82(12)	O^{2-}
O19	4*e*	0.5	0.163(2)	0.75	1	0.083(6)	0.43(3)	H_2O
O20	8*f*	0.276(5)	0.161(4)	0.803(4)	0.5	0.083(6)	0.92(5)	H_2O
O21	4*e*	0	0.176(6)	0.75	1	0.083(6)	0.00	H_2O
O22	4*e*	0.5	0.319(4)	0.75	0.5	0.083(6)	0.00	H_2O

Table 5. Selected interatomic (bond) distances (in Å) for ranunculite.

U1–O6	1.79	P1–O10	1.52	P2–O11	1.52
U1–O7	1.79	P1–O12	1.52	P2–O17	1.52
<U1–O_{Ur}>	1.79	P1–O16	1.52	P2–O18	1.53
U1–O14	2.29	P1–O13	1.521	P2–O8	1.53
U1–O17	2.30	Al1–O11	1.95	Al2–O20	1.93
U1–O16	2.33	Al1–O11	1.95	Al2–O7	1.95
U1–O13	2.35	Al1–O12	1.95	Al2–O10	1.96
U1–O18	2.35	Al1–O12	1.95	Al2–O15	1.96
<U1–O_{eq}>	2.32	Al1–O4	1.96	Al2–O9	1.97
U2–O1	1.8	Al1–O4	1.96	Al2–O8	1.98
U2–O3	1.8				
<U2–O_{Ur}>	1.8		Al3–O9	1.93	
U2–O14	2.24		Al3–O20	1.94	
U2–O14	2.31		Al3–O5	1.94	
U2–O17	2.52		Al3–O15	1.97	
U2–O11	2.70		Al3–O19	1.97	
U2–O13	2.70				
U2–O12	2.77				
<U2–O_{eq}>	2.49				

Notice: the restrictions on bond lengths were applied during the structure refinement.

Table 6. Selected data for ranunculite and phuralumite from Kobokobo.

	Ranunculite	**Phuralumite**
Unit-cell volume [$Å^3$]	3553	2517
n H_2O (total)	10.5	11
$D_{calc.}$, including theor. H [g cm^{-3}]	3.4042	3.394
Structural complexity*, $I_{G,total}$ [bits/unit-cell]	886.64	1388.30

* – including theoretical H atoms contribution

Table 7. Actinide-bearing and associated minerals from Kobokobo pegmatite and their structural and chemical complexity measures.

Mineral	References	Spgr.	V [Å]	v	I_G [bits/atom]	$I_{G,total}$ [bits/unit cell]	I_{Chem} [bits/formula]
Althupite	[1]	$P\bar{1}$	2434	130	6.04	784.91	164.44
Furongite	[2]	$P\bar{1}$	2746	148	6.21	920.00	175.29
Kamitugaite	[3]	$P\bar{1}$	1553	96	5.59	536.16	121.71
Phuralumite	[4]	$P2_1/n$	2517	148	5.21	771.00	91.01
Ranunculite	[5]	$P2_1/c$	596	108	4.83	521.53	121.42
Threadgoldite	[6]	$C2/c$	3363	104	4.70	488.85	67.60
Upalite	[7]	$P2_1$	736	116	4.89	567.53	70.81
Phosphuranylite	[8]	$Cmcm$	3765	152	5.04	765.69	128.31
Metavanmeersscheite	[9]	$Fddd$					58.09
Vanmeersscheite	[10]	$P2_1mn$	2008	104	4.89	508.85	66.13
Kobokoboite	[11]	$P\bar{1}$?	621				104.91
Eylettersite	[12]	$R\bar{3}m$	706				45.42

[1] – Piret and Deliens (1987), [2] – Dal Bo *et al.* (2017a), [3] – Plášil (2017), [4] – Dal Bo *et al.* (2017b), [5] – this paper, [6] – Khosrawan-Shazedj (1982), [7] – Piret and Declerq (1983), [8] – $K_2Ca[(UO_2)_7(PO_4)_4O_2(OH)_2](H_2O)_8$ – the electroneutral formula proposed for phosphuranylite, which was derived from new structure determinations (unpublished data of authors), [9] – Piret and Deliens (1982), [10] – Piret and Deliens (1982), [11] – Mills *et al.* (2010), [12] – Van Wambeke (1972).